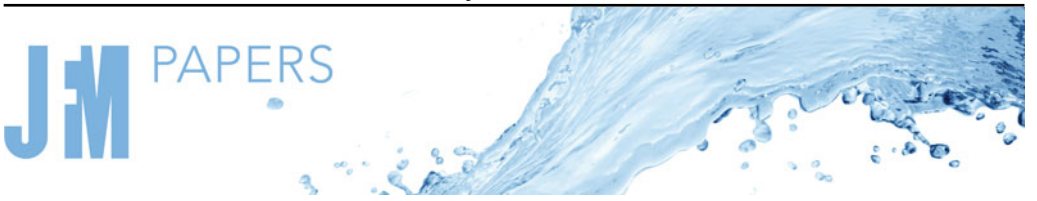
J. Fluid Mech. (2025), *vol.* 1024, A19, doi:10.1017/jfm.2025.10919



Settling of actively buoyant particles

Erika S. MacDonald[1] **and Nicholas T. Ouellette**[1]

[1]The Bob and Norma Street Environmental Fluid Mechanics Laboratory, Department of Civil and Environmental Engineering, Stanford University, Stanford, CA 94305, USA

Corresponding authors: Nicholas T. Ouellette, nto@stanford.edu; Erika S. MacDonald, emacd@stanford.edu

(Received 7 August 2025; revised 1 October 2025; accepted 3 November 2025)

Not all particulate matter carried by fluid flows has constant buoyancy. In some cases, the buoyancy of a particle can change dynamically based on the local flow. We refer to this phenomenon as 'active buoyancy.' Although actively buoyant particles are found throughout nature, their dynamics is not well understood, particularly when they are also highly inertial. Motivated by the problem of the transport of firebrands in wildfires, whose effective buoyancy is modulated by conductive and convective heat transfer to the surrounding fluid, we conducted a series of experiments to investigate the effects of active buoyancy on particle settling in quiescent fluid. We find that, depending on the control parameters, active buoyancy can either hinder or enhance settling, in some cases to a large extent. The details of this settling modulation, however, cannot be simply captured by any single control parameter. Analysis of the trajectories of the falling particles showed that they fall along nearly sinusoidal paths even though the particle Reynolds number is higher than expected for this regime, suggesting that active buoyancy may act to stabilise their wakes. Our results suggest both that models of actively buoyant particles such as firebrands must account for the effects of active buoyancy and that there is still much to be understood about the behaviour of these complex particles.

Key words: particle/fluid flows, geophysical and geological flows, convection

1. Introduction

Fluid flows in both the natural world and in engineering applications are rarely homogeneous; rather, they often carry suspended particulate material. The dynamics of such multiphase flows can be extremely complex (Balachandar & Eaton 2010), even when the particles themselves are simple and passively advected by the flow. In the more general case where the particles are 'active' and can generate their own forces or modulate their

© The Author(s), 2025. Published by Cambridge University Press. This is an Open Access article, distributed under the terms of the Creative Commons Attribution-NonCommercial licence (https://creativecommons.org/licenses/by-nc/4.0/), which permits non-commercial re-use, distribution, and reproduction in any medium, provided the original article is properly cited. The written permission of Cambridge University Press or the rights holder(s) must be obtained prior to any commercial use.

https://doi.org/10.1017/jfm.2025.10919 Published online by Cambridge University Press

interaction with the fluid in addition to being carried by the flow, we have little general predictive capability. A particular example of such active particles that is our focus here are those whose effective buoyancy can change in response to the local flow around them.

Actively buoyant particles are not uncommon, and include, for example, living 'particles' such as algae or plankton that modulate their buoyancy for a variety of reasons (Reynolds, Oliver & Walsby 1987; Gemmell *et al.* 2016; Arrieta *et al.* 2020). Our primary motivation for studying actively buoyant particles, however, is the problem of so-called spot ignition by transported firebrands in wildfires. Firebrands are small pieces of burning or smouldering material that are ejected from actively burning regions. If firebrands are sufficiently lofted and are entrained into the atmospheric boundary layer, they can be transported far downstream of the burning front, potentially leading to the ignition of 'spot fires' in distant locations (Koo *et al.* 2010; Fernandez-Pello 2017; Manzello *et al.* 2020). Predicting the landing sites of firebrands is critically important for wildfire containment and mitigation, but remains an unsolved challenge (Koo *et al.* 2010; Thurston *et al.* 2017; Or *et al.* 2023).

Fire spotting is often broken into three logically distinct elements: generation of firebrands in the burning part of the fire, their transport downstream and the ignition of unburned fuel at the landing site (Koo *et al.* 2010). Firebrand generation and fuel ignition are primarily combustion problems, and are not our focus here. The transport of firebrands, however, is a complex multiphase flow problem. The current state of the art in modelling firebrand transport makes a number of assumptions that may not be valid (Tohidi & Kaye 2017). For example, it is common to assume that firebrands always travel at their terminal velocity relative to the wind speed (Thomas, Sharples & Evans 2020), and their drag is estimated using empirical drag coefficients determined at isothermal conditions (Albini, Alexander & Cruz 2012; Dal-Ri Dos Santos 2023). These assumptions have been shown to overestimate transport distances when compared with measurements (Thomas *et al.* 2020). The firebrands relevant to spotting continue to undergo combustion reactions as they travel; however, the effect of these reactions is often only incorporated by a modelled mass loss and temperature change (Fernandez-Pello 2017), without consideration for how these characteristics affect the particle motion aside from modifying the particle size. Importantly, heat transfer from the particle to the air and its consequences is largely neglected, even though fundamental studies of heated particles moving in flows have demonstrated that there can be strong two-way coupling effects on the local particle and fluid motion (Frankel *et al.* 2016; Zamansky *et al.* 2016).

A potentially key factor that is missing from current models is the dynamic modification of the firebrand's effective buoyancy due to heat transfer. The elevated temperature of the firebrand relative to the surrounding air far from the burning fire makes them more buoyant than would be expected since they can heat a 'jacket' of fluid around them through thermal conduction that is then less dense than the rest of the air. Additionally, this heated air will tend to rise, exerting an upward drag force on the particle while also changing the viscous drag exerted on the particle from the surrounding cold fluid. Convection, however, can act to suppress this enhanced effective buoyancy and modulated drag by advecting away the scalar that is its source and thinning the low-density jacket, but in a way that depends on the local flow. These density effects are illustrated schematically in figure 1.

Some theoretical results exist for the drag on a heated sphere in the limit of low particle Reynolds number (Mograbi & Bar-Ziv 2005*a*,*b*; Ganguli & Lele 2019, 2020) or in the Boussinesq limit (Kotouč *et al.* 2009), and demonstrate that, even for these simplified cases, the problem is complex. Firebrands, however, are not in either of these limits. Typical firebrands in wildfires have linear sizes of a few centimetres (Manzello,

https://doi.org/10.1017/jfm.2025.10919 Published online by Cambridge University Press

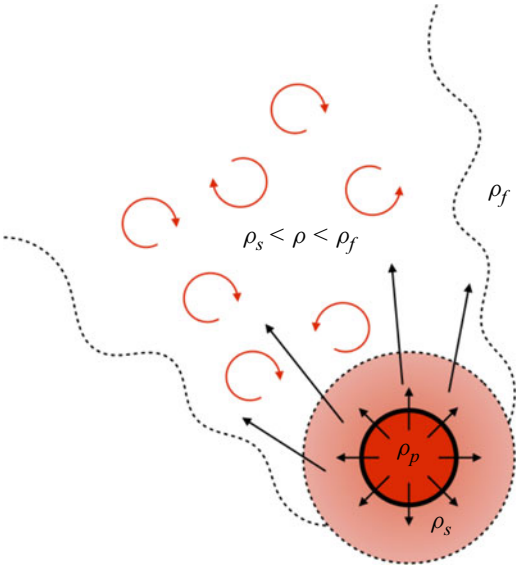


Figure 1. Schematic of the density field near an actively buoyant particle. The particle density ρ_p is larger than the fluid density ρ_f. Due to the buoyant scalar attached to the particle that mixes into the fluid directly around the particle, there is a 'jacket' of fluid of density $\rho_s < \rho_f$ around the particle that can change the effective density of the particle. Because of relative motion between the particle and the fluid and the tendency of the lightweight jacket fluid to rise, however, convection will strip this lighter fluid away into a wake behind the particle where the density ρ is spatially dynamic and lies between ρ_s and ρ_f, further changing the effective density and the drag on the particle.

Maranghides & Mell 2007) and terminal velocities of a few to tens of metres per second (Sánchez Tarifa *et al.* 1965; Oliveira *et al.* 2014; Thurston *et al.* 2017; Thomas *et al.* 2020), suggesting particle Reynolds numbers of order 10^4, far from the creeping-flow limit. By the same token, their typical temperatures of 500−700 °C (Anthenien, Tse & Fernandez-Pello 2006) suggest that the heat transfer from a firebrand to the surrounding air is far from Boussinesq. Thus, appropriately modelling the behaviour of a transported firebrand requires working in this difficult regime where common simplifying assumptions are not valid.

Since a first-principles theoretical analysis of the dynamics of an actively buoyant particle in the relevant parameter range is therefore intractable, we conducted a series of experiments to measure the settling of actively buoyant particles in a quiescent fluid. Before presenting our results, we first identify the relevant non-dimensional parameter space that characterises this system. We then describe our experimental methods, including our choice of buoyant scalar and the fabrication of appropriate particles, before moving on to our results. We find that the settling velocity of our actively buoyant particles can be either suppressed or enhanced relative to what would be expected for an inert particle, but that there is no simple dependence of the results on a single control parameter. We also analyse the trajectories of the settling particles. We find that these trajectories are well described as single-mode sinusoids with an approximately constant Strouhal number even though the Reynolds number range would suggest that the trajectories ought to be more complex. Taken together, our results indicate that the effects of active buoyancy on the particle dynamics are complex and not small, and thus that understanding the behaviour of such particles is ripe for further study.

https://doi.org/10.1017/jfm.2025.10919 Published online by Cambridge University Press

2. Methods

2.1. *Relevant parameters*

Even the simplest situation of an actively buoyant particle settling in a quiescent fluid is governed by a large number of parameters. The background fluid is characterised by its mass density ρ_f and dynamic viscosity μ. Likewise, the particle has a density ρ_p and a diameter d. Because in general $\rho_f \neq \rho_p$, buoyancy effects will be relevant so that the gravitational acceleration g must enter the problem. Given our motivation, we consider the active buoyancy of the particle to arise due to an internal reservoir of a scalar associated with the particle that can mix into the surrounding fluid. This scalar is characterised by a density ρ_s, which we define as the density of the fluid–scalar mixture when the scalar takes its peak value (e.g. the density of air heated to the temperature of a firebrand in the wildfire context), and a diffusion constant κ. Note that we assume both that the scalar reservoir is effectively infinite and that the particle density is constant in time; although these approximations are never strictly valid, in many practical situations these properties change on much slower time scales than the particle velocity. In the settling problem, we seek to determine the terminal settling velocity w as a function of these input parameters. Application of the Buckingham Pi theorem indicates that the non-dimensional settling velocity can be written as a function of four non-dimensional input parameters.

Previous work on the settling of finite-size particles has indicated that mass effects and size effects are important, and are not interchangeable (Cabrera-Booman, Plihon & Bourgoin 2024); we therefore choose two of these input parameters to be the specific gravity $\Gamma = \rho_p/\rho_f$ and the Galileo number

$$Ga = \sqrt{\frac{gd^3\rho_f|(\rho_p - \rho_f)|}{\mu^2}} = \sqrt{\frac{gd^3\rho_f^2|\Gamma - 1|}{\mu^2}}, \tag{2.1}$$

which compares the effects of the (passive) particle buoyancy and viscous effects. To capture effects of the buoyancy due to the scalar (that is, the active contribution to the particle buoyancy), we use the particle Grashof number

$$Gr_p = \frac{gd^3\rho_f(\rho_f - \rho_s)}{\mu^2}, \tag{2.2}$$

where we have assumed that the scalar density varies linearly with concentration. We refer to Gr_p as a particle Grashof number since we use the particle length scale d rather than a (larger) length scale defined by the buoyant plume attached to the particle. Finally, we also consider the Prandtl number $Pr = \mu/(\rho_f\kappa)$ (or, equivalently, the Schmidt number Sc if the scalar is not heat).

We non-dimensionalise the settling velocity using what is sometimes referred to as the settling number $Sv = w/w_{ex}$, where w_{ex} is the expected settling velocity. If the particle were both small and close to neutrally buoyant, it could be appropriate to set w_{ex} to the Stokes settling velocity. In the more general case where the particle inertia is non-negligible, it is more appropriate to define

$$w_{ex} = \sqrt{\frac{4gd(\rho_p - \rho_f)}{3\rho_f C_d}}, \tag{2.3}$$

where C_d is a drag coefficient. In general, for passive particles, C_d depends on both Ga and Γ. Here, we use the recent parameterisation reported by Cabrera-Booman *et al.* (2024) for C_d and therefore w_{ex}, as it conveniently expresses C_d purely as a function of Ga. This parameterisation is given by

https://doi.org/10.1017/jfm.2025.10919 Published online by Cambridge University Press

$$C_d(Ga) = \frac{4}{3}\left(\frac{0.0258Ga^{2.6973} + 2.81Ga^{2.0306} + 18Ga^{1.364} + 405}{Ga(22.5 + Ga^{1.364})}\right)^2. \tag{2.4}$$

Other choices for the relevant non-dimensional parameters are, of course, possible. It is common, for example, to define a particle Reynolds number $Re_p = \rho_f w d/\mu$. In our case, w is an output parameter and emerges from a steady-state balance between the forces on the particle rather than being set as the result of an externally imposed flow, and so Re_p should also be considered to be an output. Here, we prefer to use Sv as the non-dimensional output variable, as it directly indicates whether the settling velocity is expected or anomalous. Previous studies of heated particles in external flows have shown the importance of the parameter Gr_p/Re_p^2 in controlling the heat transfer between the particle and the fluid (Acrivos 1958; Mograbi & Bar-Ziv 2005*a*,*b*). This ratio, which can be thought of as a Richardson number, distinguishes the limits of heat transfer by natural convection ($Gr_p/Re_p^2 \gg 1$) or by forced convection ($Gr_p/Re_p^2 \ll 1$). When $Gr_p/Re_p^2 \sim O(1)$, the case of mixed convection, the dynamics is expected to be especially complex (Mograbi & Bar-Ziv 2005*a*,*b*; Ganguli & Lele 2020). Although we return to this parameter and the convective regime below, we again note that it is not a control parameter as such since it mixes input (Gr_p) and output (Re_p) variables.

2.2. *Buoyancy source and particles*

By defining the non-dimensional parameter space for this problem, we can take advantage of dynamical similitude to choose a combination of particle, buoyancy source and carrier fluid that allows the application of convenient experimental techniques while still making it possible to examine the fundamental physics governing the behaviour of actively buoyant particles. We use water as the working fluid, both because it is compatible with a wide range of flow visualisation techniques and because its density and viscosity relative to those of air slow down settling time scales, allowing for more precise measurements. Water does make it difficult, however, to use temperature as the buoyancy-modulating scalar, for several reasons. The relatively high thermal conductivity of water means that heat transfer from a hot particle is fairly efficient even by conduction, so that it is difficult to fabricate a small particle with enough internal heat reserves to remain at an elevated temperature for any appreciable length of time. And second, water remains a liquid only up to a temperature of 100 °C, and the density of 100 °C water is only approximately 4 % less than that of room-temperature water. Thus, the excess buoyancy that can be generated by heating water is fairly small.

Instead of temperature, we use ethanol as our source of buoyancy. Like temperature, ethanol concentration is a diffusing scalar field, since ethanol is fully soluble in water. However, the diffusion of ethanol is slower than the diffusion of heat in water, so that elevated levels of ethanol concentration around a particle will persist longer than elevated temperatures. Pure ethanol also has a specific gravity of 0.79, so that the excess buoyancy that can be generated using ethanol is much larger than what can be generated using temperature in water. This choice means that we are essentially considering compositional convection rather than thermal convection near the particle (and so, for that reason, we report the Schmidt number Sc rather than the Prandtl number Pr below); however, the underlying physics is sufficiently similar that our results will still have bearing on the wildfire problem. And even though the density contrast between ethanol and water is somewhat smaller than what would be expected for a several-hundred-degree temperature difference in air, it is still sufficiently high to fall in the strongly non-Boussinesq regime. Using ethanol as the buoyancy source imposes requirements on the particles that can

https://doi.org/10.1017/jfm.2025.10919 Published online by Cambridge University Press

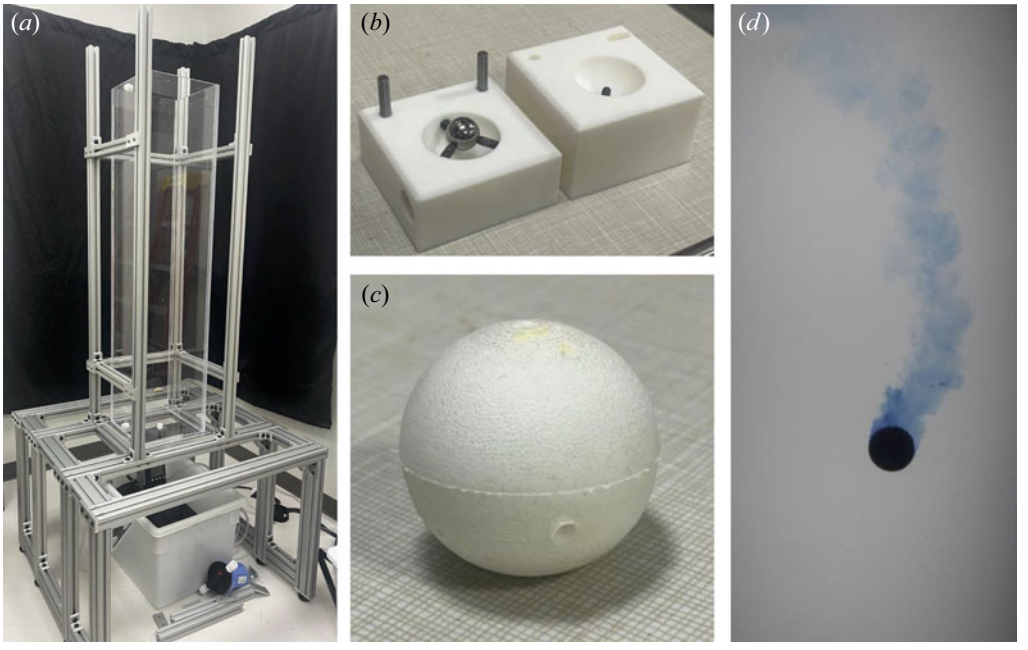


Figure 2. (*a*) Photograph of the settling chamber used in these experiments. (*b*) An example 3D-printed mould used for casting the foam particles. The core ball bearing is held in place by alignment screws arranged in a tetrahedral configuration. The two halves of the mould are precisely aligned with pins. (*c*) An example completed particle. (*d*) An example image of a falling particle charged with ethanol. For qualitative visualisation of the scalar wake in this example, the ethanol has been dyed blue.

be used: we need particles that can hold a reservoir of ethanol that can diffuse into the surrounding water, ideally slowly enough that the reservoir does not deplete rapidly compared with the time scale of the experiments. In addition, as we wish to study settling, the particles must be dense enough that they remain negatively buoyant in water even when their ethanol reservoir is full.

To meet these requirements, we developed a method to fabricate porous particles from a spongy open-cell polyurethane foam that is both water and ethanol compatible. By soaking the particle in a water/ethanol solution of fixed concentration, we could 'charge' the particle with a reservoir of a passive scalar with a specified ρ_s, which then diffused out of the particle when placed in water. As long as the particle was sufficiently large, this internal ethanol reservoir did not appreciably deplete over the course of each experiment. However, because the foam has only a small mass, an ethanol-charged foam particle is positively buoyant in water. We therefore used a core–shell design, casting the foam around a small steel core to add mass. By varying the size of the steel core, we could vary ρ_p (which we defined as the net mass of the particle divided by its total volume) independently of d.

Specifically, we used 440C stainless steel ball bearings of various sizes as the particle cores. The outer shell was fabricated from a castable polyurethane foam (Smooth-On FlexFoam-iT! 6). To ensure the ball bearing was centred within the foam shell, we designed a custom 3D-printed mould (figure 2*b*). The mould used four screws arranged in a tetrahedral configuration, with each screw bottoming out to suspend the ball bearing precisely at the centre. Two alignment pins were included to ensure alignment between the top and bottom hemispheres of the mould, which were fit together while the initially liquid foam precursor expanded and cured. An example of the final particle is shown in figure 2(*c*), and an example of a particle settling while loaded with ethanol is shown in

https://doi.org/10.1017/jfm.2025.10919 Published online by Cambridge University Press

figure 2(*d*). As can be seen in figure 2(*c*), removing the screws used to hold the ball-bearing core during curing does create four small holes in the particle, and the two-part mould leaves an unavoidable ring around the equator of the particle. These features are small compared with the particle dimensions, however, and so we do not anticipate that they contribute in any significant way to the particle dynamics. Additionally, we did not observe significant differences in the settling behaviour of the particles when dropped in different orientations. Still, to control for any slight systematic differences as a function of these surface imperfections, we kept the initial orientation of the particles the same for all the results reported below.

2.3. *Experimental set-up*

To study actively buoyant particle settling, we conducted experiments using four particle types. The outer diameter of each particle mould was the same in all cases (2.19 cm), but we used four different ball-bearing cores (with diameters of 0.87, 0.95, 1.11 and 1.27 cm). We loaded the particles with five different water–ethanol solutions: 0 % (pure water), 25 %, 50 %, 75 % and 100 % ethanol by volume. The mass densities of these mixtures (corresponding to ρ_s in our definitions above) are 1.00, 0.97, 0.93, 0.87 and 0.79 g cm^{-3}, respectively. We note that the diffusion constant for a water–ethanol mixture is a function of the ethanol concentration; thus, the Schmidt number for each of the cases differed. In our experiments, however, we could not change Sc independently from Gr_p, since we set each by varying the concentration of the ethanol solution. When loaded with fluid, we found that the particles swelled somewhat, so that their diameter was larger than that of the mould. We also found that the swelling was weakly dependent on the ethanol concentration. We therefore measured the volume of each loaded particle using Archimedes' principle; this method was more accurate than a direct measurement of particle diameter with callipers, given that the particles were soft. We also measured the mass of each loaded particle using a precision scale, allowing us to compute ρ_p for each experimental case. In table 1, we report the ranges of the control parameters spanned in our experiments.

To contextualise these values, and in particular the seemingly very high Grashof numbers, we note again that typical firebrands have sizes of a few centimetres (Manzello *et al.* 2007), temperatures of 500−700 °C (Anthenien *et al.* 2006) and are made of wood or similar organic material, giving $Gr_p \sim O(10^6)$ and $Ga \sim O(10^4)$. The values of Γ and Sc in our experiments are, however, quite different from the firebrand case.

In each experimental run, the particle was released from rest into a tank of quiescent water, as shown in figure 2(*a*). The tank had a square cross-section measuring 25.4 cm on a side, and was 127 cm tall. These dimensions were chosen to minimise potential wall effects on the settling (Miyamura, Iwasaki & Ishii 1981; Chhabra 1995) and to be large enough to allow the particles to reach their terminal velocity well before hitting the bottom (Khatmullina & Isachenko 2017; Wang *et al.* 2021). Particles were released through a funnel to ensure a consistent initial location, and the initial orientation of the particle was controlled in order to minimise any variability due to small surface deformities resulting from the screw locations in the casting mould. We observed that the particles did not tumble or rotate as they fell, suggesting both that any such deformities did not have a large effect on the particle dynamics and that the centre of mass of the particles was co-located with their geometric centre.

A LED light sheet illuminated the particle from behind, and a grey scale CMOS camera (FLIR Flea3) imaged the particles settling at 100 frames per second. The camera was positioned far enough below the funnel that the particles had reached their terminal

https://doi.org/10.1017/jfm.2025.10919 Published online by Cambridge University Press

d_{core}/d_{mold}	Γ	Ga	Gr_p	Sc
0.40	1.32	5.54×10^3	0	0.81×10^3
0.40	1.29	5.68×10^3	0.59×10^7	2.1×10^3
0.40	1.22	5.42×10^3	1.4×10^7	3.0×10^3
0.40	1.13	4.55×10^3	2.5×10^7	1.4×10^3
0.40	1.03	2.27×10^3	4.0×10^7	0.95×10^3
0.43	1.46	6.62×10^3	0	0.81×10^3
0.43	1.40	6.70×10^3	0.60×10^7	2.1×10^3
0.43	1.31	6.46×10^3	1.4×10^7	3.0×10^3
0.43	1.21	5.76×10^3	2.5×10^7	1.4×10^3
0.43	1.10	4.29×10^3	4.0×10^7	0.95×10^3
0.51	1.83	8.81×10^3	0	0.81×10^3
0.51	1.70	8.87×10^3	0.59×10^7	2.1×10^3
0.51	1.56	8.66×10^3	1.4×10^7	3.0×10^3
0.51	1.41	8.10×10^3	2.5×10^7	1.4×10^3
0.51	1.26	7.03×10^3	4.0×10^7	0.95×10^3
0.58	2.25	1.09×10^4	0	0.81×10^3
0.58	2.08	1.10×10^4	0.59×10^7	2.1×10^3
0.58	1.89	1.09×10^4	1.4×10^7	3.0×10^3
0.58	1.70	1.05×10^4	2.5×10^7	1.4×10^3
0.58	1.51	0.98×10^4	4.0×10^7	0.95×10^3

Table 1. Control parameters for the different experimental cases considered. Here, d_{core} is the diameter of the inner ball-bearing core in each particle, and $d_{mold} = 2.19$ cm is the diameter of the particle mould (and so the outer diameter of the dry particle).

velocity in the imaging region. Two-dimensional particle trajectories were reconstructed using a predictive tracking algorithm (Kelley & Ouellette 2011), and the terminal velocity was measured by linear fits to the time series of the vertical particle position (see figure 8 below for examples of these time series). We chose to fit the time series rather than differentiating the data to avoid the amplification of any experimental error due to numerical derivatives. We performed 10 trials for each of the 20 experimental conditions. The fluid in the tank was allowed to come to rest over a period of several minutes between runs; measurements of the fluid velocity after this time period indicated that any residual fluid motion was far smaller the run-to-run variability in our experiments.

3. Results and discussion

3.1. *Settling velocity*

Our primary goal in this work is to characterise the effects of active buoyancy, as indicated by a non-zero particle Grashof number Gr_p, on the quiescent settling velocity of a particle. In figure 3, we therefore plot the settling number $Sv = w/w_{ex}$ as a function of Gr_p. As discussed above, we measured w by fitting the time series of the vertical position. We computed w_{ex} from (2.3).

The data shown in figure 3 have several intriguing features. First, for $Gr_p = 0$, corresponding to the case with no active buoyancy, $Sv \approx 0.8$, indicating that even without active buoyancy our particles settle approximately 20 % more slowly than expected. The cause of this discrepancy is not immediately clear. We note that our particle Reynolds numbers Re_p are significantly higher than those considered by Cabrera-Booman *et al.* (2024), which may explain part of the deviation; they reported results for Re_p up to

https://doi.org/10.1017/jfm.2025.10919 Published online by Cambridge University Press

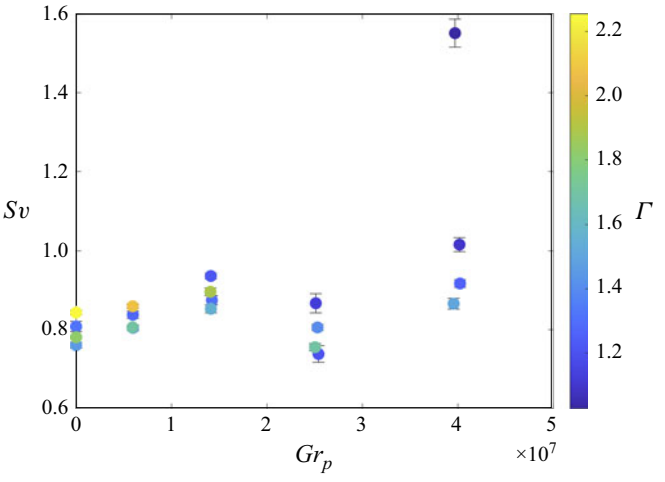


Figure 3. The settling number Sv plotted as a function of the particle Grashof number Gr_p. The colour of each data point shows the specific gravity Γ, as indicated by the colour bar. The error bars correspond to the standard error over 10 trials for each set of control parameters.

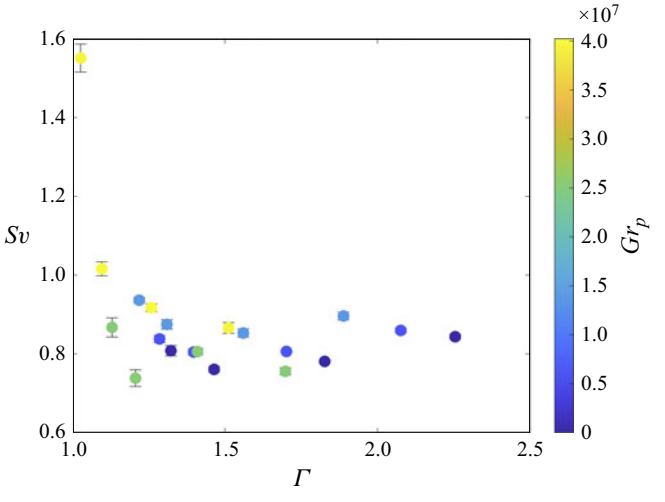


Figure 4. The settling number Sv plotted as a function of the specific gravity Γ. The colour of each data point shows the particle Grashof number Gr_p, as indicated by the colour bar. The error bars correspond to the standard error over 10 trials for each set of control parameters.

approximately 500, while our particles have $Re_p \sim O(10^4)$. Cabrera-Booman *et al.* (2024) also noted that C_d may have a systematic dependence on the specific gravity Γ that was not captured in their parameterisation, with lighter particles experiencing more drag than expected and heavier particles experiencing less drag. To investigate whether such an effect is present in our data as well, we both colour the data points in figure 3 by Γ and plot Sv as a function of Γ (coloured by Gr_p) in figure 4. Although we do observe spread in our data as a function of Γ, the overall trends are not so clear – and if anything appear to suggest the opposite of what Cabrera-Booman *et al.* (2024) observed, as Sv is larger for smaller values of Γ than for larger values.

An additional possibility is that the porosity or surface roughness of our particles or mass transfer effects may have an impact on their settling. Emadzadeh & Chiew

https://doi.org/10.1017/jfm.2025.10919 Published online by Cambridge University Press

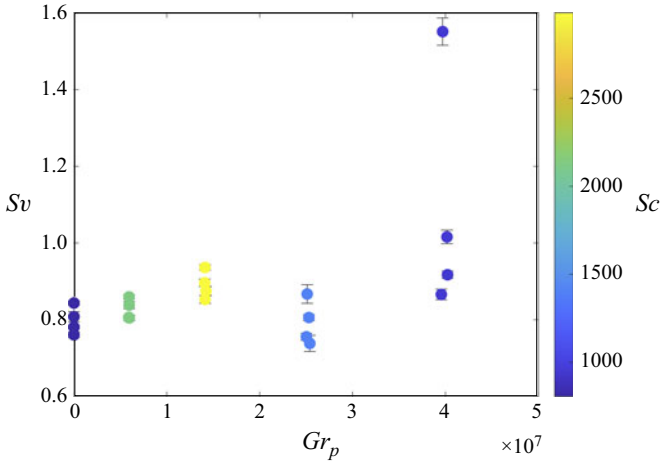


Figure 5. The settling number Sv plotted as a function of the particle Grashof number Gr_p. The colour of each data point shows the Schmidt number Sc, as indicated by the colour bar. The error bars indicate the standard error over 10 trials for each set of control parameters. Note that, although the data for each Gr_p have the same Sc, Sc in our experiments does not vary monotonically with Gr_p.

(2020) reported enhanced drag coefficients for porous particles for $Re_p > 100$, which they attributed to a combination of increased frictional drag, reduced pressure drag, a modified wake and boundary layer separation. The magnitude of increased drag observed in their experiments is consistent with the reduction in Sv that we observe for $Gr_p = 0$. However, they did not report a general parameterisation of the drag coefficient for porous particles, so we cannot directly extrapolate their results for our situation. Mass transfer also occurs on the surface of our particles, since as the ethanol mixture loaded into the particles flows out it is replaced the background pure water. This mass transfer could lead to a Stefan flow, which may affect the drag as well (Jayawickrama *et al.* 2019), although to an extent that is difficult to predict at our high particle Reynolds numbers. A potential option to at least partially account for these complications would be to define Sv using the measured settling velocity for the $Gr_p = 0$ case as the velocity scale, so that $Sv(Gr_p = 0)$ would be unity. However, as we change Gr_p by varying the ethanol concentration loaded into the particles, Ga also changes – and we expect the drag to be a function of Ga. Thus, in estimating the expected settling velocity to define Sv, we choose to use the C_d model from Cabrera-Booman *et al.* (2024) and simply compare with the $Gr_p = 0$ case as a reference point for assessing the relative influence of active buoyancy.

Independent of the lower-than-expected Sv at $Gr_p = 0$, figure 3 shows that Sv does indeed vary with Gr_p, that the settling can be either slower or faster than expected, and that this variation is non-monotonic. For $0.5 \times 10^7 < Gr_p < 1.5 \times 10^7$, Sv increases slightly relative to the $Gr = 0$ case. A slight decrease in Sv occurs around $Gr_p = 2.5 \times 10^7$, followed by a further increase in Sv dependent on Γ near $Gr_p = 4 \times 10^7$, which is more pronounced for particles with Γ closer to unity. A potential explanation for the non-monotonic behaviour we observe may be Schmidt number dependence. As described above, the primary way we vary Gr_p is by changing the concentration of the ethanol solution loaded into the particles, which changes ρ_s. Here, Gr_p increases monotonically as this concentration increases. However, the diffusion constant for ethanol–water mixtures does not vary monotonically with concentration (Pratt & Wakeham 1974), meaning that our Schmidt numbers do not vary monotonically with Gr_p, as shown in figure 5.

https://doi.org/10.1017/jfm.2025.10919 Published online by Cambridge University Press

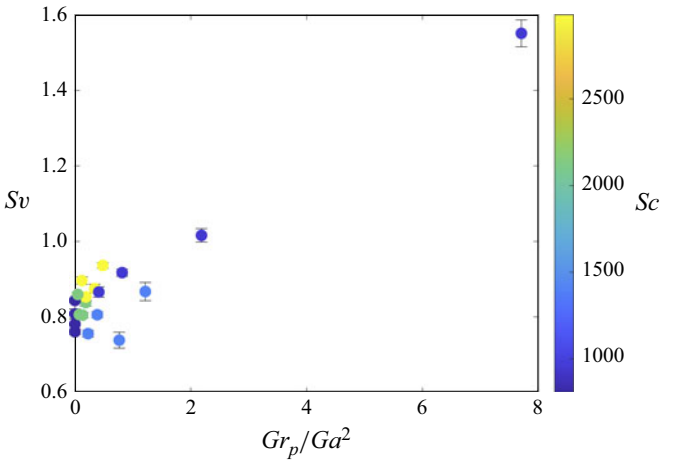


Figure 6. The settling number Sv plotted as a function of the ratio of the particle Grashof number Gr_p to the square of the Galileo number Ga. This composite parameter is equivalent to the ratio of the density anomaly due to the scalar and the density anomaly due to the particle (see text). The colour of each data point shows the Schmidt number Sc, as indicated by the colour bar. The error bars correspond to the standard error over 10 trials for each set of control parameters.

Given the lack of theory for this inertial, non-Boussinesq regime and the co-variation of Sc and Gr_p in our experiments, we cannot at present clarify the distinct dependence of Sv on Sc.

This lack of theory also generally prevents us from exploring any dependence of Sv on combinations of our four control parameters. Nevertheless, we do consider the variation of Sv with the composite parameter Gr_p/Ga^2, as shown in figure 6, because its limits are physically interpretable. As can readily be seen from their definitions

$$\frac{Gr_p}{Ga^2} = \frac{\rho_f - \rho_s}{\rho_p - \rho_f}, \tag{3.1}$$

and can thus be interpreted as the ratio of the density anomaly due to the scalar attached to the particle (which contributes to the active, dynamical part of the particle's effective buoyancy) and the density anomaly due to the intrinsic particle density (which is purely passive and static). As seen in figure 6, we observe an approximately linear relationship between Sv and Gr_p/Ga^2 in our parameter range, with a cross-over from $Sv < 1$ to $Sv > 1$ at $Gr_p/Ga^2 \approx 2$. This result suggests that the enhancement of the settling velocity begins to occur when the active buoyancy dynamics begins to outweigh the passive contribution. However, this result also has other possible interpretations. We note that Gr_p/Ga^2 can also be written as $\Lambda/(\Gamma - 1)$, where $\Lambda = (\rho_f - \rho_s)/\rho_f$ is a parameter that can be used to assess how non-Boussinesq the density perturbations due to the scalar are (Ganguli & Lele 2019). As Λ, and therefore Gr_p/Ga^2, grows, we might expect the scalar field shed from the particle to begin to affect its momentum directly via a momentum flux rather than only indirectly through a renormalisation of its effective density.

As a final way to characterise our settling results, in figure 7 we plot Sv as a function of the mixed-convection parameter Gr_p/Re_p^2. As discussed above, this parameter indicates the relative strength of free and forced convection, and thus brings in some of the dynamics. Although the results should be interpreted with some caution, given that the measured settling velocity w appears in both Sv and Re_p, figure 7 suggests that the

https://doi.org/10.1017/jfm.2025.10919 Published online by Cambridge University Press

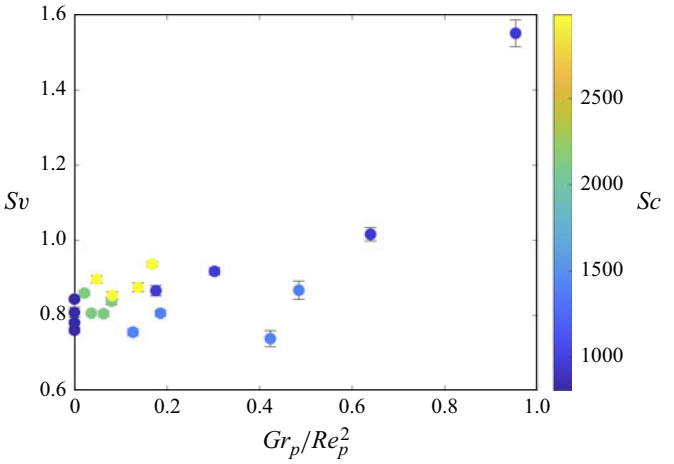


Figure 7. The settling number Sv plotted as a function of the ratio of the particle Grashof number Gr_p to the square of the particle Reynolds number Re_p. For $Gr_p/Re_p \ll 1$, the scalar wake behind the particle is expected to result from free convection, while for $Gr_p/Re_p \gg 1$ it is expected to result from forced convection. The case $Gr_p/Re_p \approx 1$ corresponds to the complex, mixed-convection case (see text). The colour of each data point shows the Schmidt number Sc, as indicated by the colour bar. The error bars correspond to the standard error over 10 trials for each set of control parameters.

enhanced settling of our actively buoyant particles is most pronounced when $Gr_p/Re_p^2 \sim 1$, indicating strong and potentially nonlinear coupling between free and forced convection (Ganguli & Lele 2020).

3.2. *Particle trajectories*

In addition to characterising the particle settling velocity, we also investigated the particle paths themselves. As can be seen in figure 2(*d*), our particles do not follow straight paths; rather, we observe oscillatory behaviour that is nearly confined in a single two-dimensional plane (sometimes with some small out-of-plane motion as well) in all cases. These zig-zag paths are not unexpected, given the particle Reynolds numbers ($Re_p \sim O(10^4)$) with which our particles fall. A significant amount of previous work has characterised the paths of falling objects (Ern *et al.* 2012) as the particle Reynolds number increases, which can be described as arising from instabilities of the inertial wake shed from the falling particle (Uhlmann & Dušek 2014; Dušek 2017). The resulting trajectories can be straight, angled, oscillatory or even chaotic. Our actively buoyant particles, however, are more complex: in addition to the typical inertial wake, they also leave behind a density wake. The interaction of this density anomaly with the fluid and particle inertia may potentially affect the wake instabilities that drive the deviation of a settling particle from a straight path (Ern *et al.* 2012; Uhlmann & Dušek 2014; Dušek 2017).

In figure 8, we show the trajectories for the set of ten experiments with $Gr_p = 4.0 \times 10^7$, $Ga = 7.03 \times 10^3$, $\Gamma = 1.26$ and $Sc = 950$. Although we only show trajectories for this set of control parameters, they are qualitatively similar for all the other cases we considered. It is immediately clear from figure 8(*a*) that the particles do not fall along a straight path, but rather oscillate. This oscillation, however, occurs only the direction perpendicular to gravity; as shown in figure 8(*b*), the vertical position of the particle is linear in time (justifying our choice to extract particle velocities via linear fits rather than numerical differentiation). The oscillations we observe are very nearly single-mode sinusoids.

https://doi.org/10.1017/jfm.2025.10919 Published online by Cambridge University Press

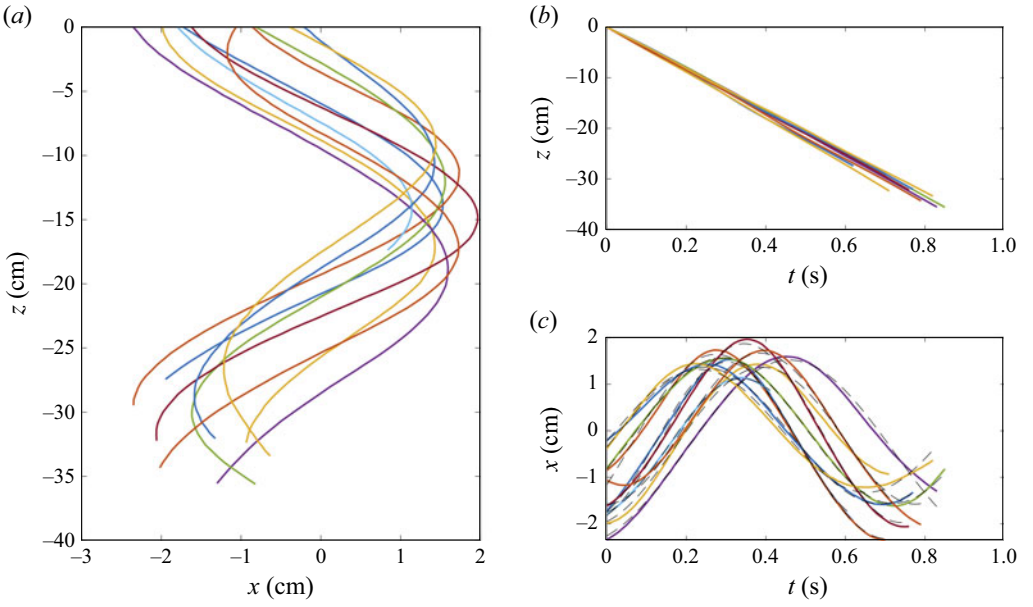


Figure 8. (*a*) Reconstructed trajectories of falling particles for ten experimental trials with $Gr_p = 4.0 \times 10^7$, $Ga = 7.03 \times 10^3$, $\Gamma = 1.26$ and $Sc = 950$. These particles had a diameter of 2.69 cm. Here, z is aligned with the gravity direction (with the acceleration due to gravity pointing in the $-\hat{\mathbf{z}}$ direction) and x is an orthogonal direction. Each trajectory is shifted so that $x = 0$ corresponds to its mean horizontal position and $z = 0$ corresponds to its initial detected location; these origins have no other physical meaning. Additionally, for ease of visualisation, some trajectories have been flipped across the x axis so that all of the trajectories appear to move initially in the positive x direction. (*b*) Time series of z for each of the ten trials. (*c*) Time series of x for each of the ten trials. Each trajectory is plotted in the same colour in (*a*), (*b*) and (*c*). The black dashed lines in (*c*) show least-squares fits of single-mode sinusoids to the time series of the horizontal position (see text for more details).

This result is somewhat surprising, as our Ga and Γ values are in the regime where we would expect chaotic trajectories (Uhlmann & Dušek 2014; Dušek 2017; Cabrera-Booman *et al.* 2024). It is possible that the shed scalar wake behind the particle, which, like the momentum wake, moves in the direction anti-parallel to gravity, may have a stabilising effect on any path instabilities. We do, however, also observe similar behaviour for the case of $Gr_p = 0$, suggesting (similar to the smaller-than-expected Sv for $Gr_p = 0$ discussed above) that other effects such as porosity may also be a factor in controlling the behaviour of the particles.

To extract a frequency f for the oscillations, we fit the time series of the horizontal particle position x to functions of the form $\cos(2\pi ft)$; figure 8(*c*) shows that these fits capture the observed behaviour very accurately. We then non-dimensionalised the frequencies to define a Strouhal number $St = fd/w$ for each set of control parameters. In figure 9, we plot St as a function of Ga. Although there is scatter in the data and potentially different behaviour for $Ga < 3000$, our results are consistent with a constant Strouhal number of approximately 0.05. There is also no apparent trend in the results as a function of Gr_p. Similar St values have been reported previously for inert settling spheres (Ern *et al.* 2012), although again for lower Ga ranges. These St values are thus again consistent with the hypothesis that the active buoyancy in our experiments may act to suppress wake instabilities that would occur due to inertia alone.

https://doi.org/10.1017/jfm.2025.10919 Published online by Cambridge University Press

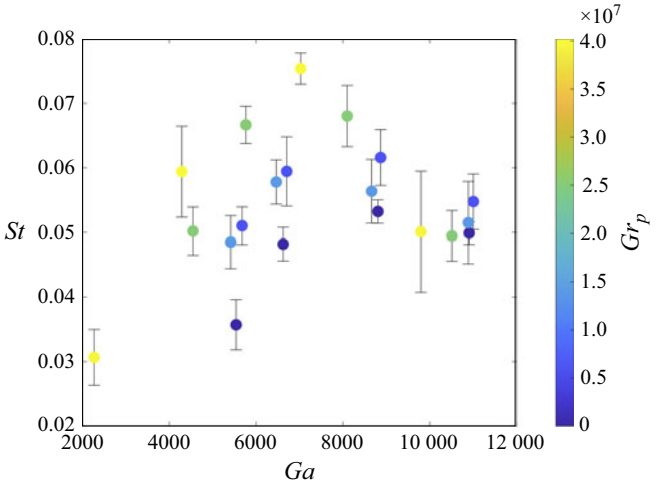


Figure 9. The Strouhal number St plotted as a function of the Galileo number Ga. The colour of each data point shows the particle Grashof number Gr_p, as indicated by the colour bar. The error bars correspond to the standard error over 10 trials for each set of control parameters.

4. Conclusions

To briefly summarise our results, we conducted a series of experiments to measure the settling behaviour of particles that released a buoyant scalar into the surrounding fluid. Because the density anomaly due to the introduction of this scalar was sourced from the particle and strongly non-Boussinesq, we refer to these particles as being actively buoyant. We found that the settling velocity could be both suppressed or enhanced relative to what would be expected for inert particles of the same size, shape and density. These deviations were not small; in particular, for our experimental case with the highest particle Grashof number and specific gravity closest to unity, we found that the settling velocity was enhanced by nearly 60 %. Given that several of our control parameters were similar to what would be expected for real firebrands, our results suggest that firebrand transport models that do not account for active buoyancy effects risk severe mis-prediction of their likely landing locations.

There is no theory currently available for how the settling velocity would be expected to depend on the governing non-dimensional parameters in the inertial, non-Boussinesq regime we studied. Indeed, our results indicate that all four control parameters (Gr_p, Ga, Γ and Sc) likely play a role in determining the settling velocity. Plotting our results as a function of the composite parameters Gr_p/Ga^2 and Gr_p/Re_p^2, which both show monotonic increase of Sv, suggests that the buoyancy of the scalar and the nature of the resulting convective flow play key roles in determining the particle settling behaviour. When combined also with the strong effects for Γ close to unity and the highly non-Boussinesq nature of the density fluctuations, we hypothesise that the direct momentum fluxes imparted on the particle by the shed scalar dominate over any simple renormalisation of the effective density of the particle. Future studies of this complex problem using, for example, numerical simulation or experimental techniques such as combined particle image velocimetry and laser-induced fluorescence could probe this hypothesis in more detail.

In contrast to the settling velocity, where the addition of active buoyancy led to significantly different values relative to the case of inert particles, we did not observe significant modifications to the trajectories of our settling particles. As would be expected

https://doi.org/10.1017/jfm.2025.10919 Published online by Cambridge University Press

for the range of Ga and Γ we investigated, the particles did not follow straight paths; instead, the particles followed nearly sinusoidal paths, with a Strouhal number similar to what would be expected for inert particles. The primary effects of active buoyancy on the trajectory structure appears to be a stabilisation of this sinusoidal regime at higher than expected Re_p, which may also arise due to the additional wake momentum flux due to the non-Boussinesq density fluctuations. Again, further detailed study of the particle wake and scalar plume shed from the particle would help to illuminate the mechanisms responsible for wake stabilisation.

Finally, we note that, although firebrand transport is our primary motivation for this work, it is far from the only situation where active, dynamically modulated particle buoyancy is an important component of the physics. The thermal activity of particles in solar receivers, for example, has been shown to play a major role in the efficacy of their energy harvesting (Frankel *et al.* 2016; Zamansky *et al.* 2016; Yang *et al.* 2022). Similarly, the heat transport in convective flows can be enhanced when they are laden with thermally expandable particles (Hu *et al.* 2021). Large-scale convection can even be generated and maintained by thermally active particles (Agasthya *et al.* 2022). And in addition to these engineering examples, the active buoyancy modulation of biological 'particles' is essential for many marine organisms (Denton 1971; Reynolds *et al.* 1987; Gemmell *et al.* 2016; Hamel *et al.* 2019; Arrieta *et al.* 2020). Our results here indicate that the behaviour of actively buoyant particles is far from simple even for the case of settling in quiescent fluid, suggesting that there is a great deal of opportunity for further study in this area, particularly as the flow field becomes more complex.

Funding. This work was supported in part by the U.S. National Science Foundation under grant number CBET-2529151.

Declaration of interests. The authors report no conflict of interest.

References

Acrivos, A. 1958 Combined laminar free- and forced-convection heat transfer in external flows. *AIChE J.* **4**, 285–289.

Agasthya, L., Bartel, A., Biferale, L., Ehrhardt, M. & Toschi, F. 2022 Large-scale convective flow sustained by thermally active Lagrangian tracers. *J. Fluid Mech.* **953**, A5.

Albini, F.A., Alexander, M.E. & Cruz, M.G. 2012 A mathematical model for predicting the maximum potential spotting distance from a crown fire. *Intl J. Wildland Fire* **21**, 609–627.

Anthenien, R.A., Tse, S.D. & Fernandez-Pello, A.C. 2006 On the trajectories of embers initially elevated or lofted by small ground fire plumes in high winds. *Fire Safety J.* **41**, 349–363.

Arrieta, J., Jeanneret, R., Roig, P. & Tuval, I. 2020 On the fate of sinking diatoms: the transport of active buoyancy-regulating cells in the ocean. *Phil. Trans. R. Soc. Lond. A* **378**, 20190529.

Balachandar, S. & Eaton, J. 2010 Turbulent dispersed multiphase flow. *Annu. Rev. Fluid Mech.* **42**, 111–133.

Cabrera-Booman, F., Plihon, N. & Bourgoin, M. 2024 Path instabilities and drag in the settling of single spheres. *Intl J. Multiphase Flow* **171**, 104664.

Chhabra, R.P. 1995 Wall effects on free-settling velocity of non-spherical particles in viscous media in cylindrical tubes. *Powder Technol.* **85**, 83–90.

Dal-Ri dos Santos, I. & Yaghoobian, N. 2023 Effects of urban boundary layer turbulence on firebrand transport. *Fire Safety J.* **135**, 103726.

Denton, E.J. 1971 Examples of the use of active transport of salts and water to give buoyancy in the sea. *Phil. Trans. R. Soc. Lond. B* **262**, 277–287.

Dušek, J. 2017 Path instabilities of axisymmetric bodies falling or rising under the action of gravity and hydrodynamic forces in a Newtonian fluid. In *Particle in Flows* (ed. T. Bodnár, G.P. Galdi & Š. Nečasová), pp. 397–451. Springer International Publishing.

Emadzadeh, A. & Chiew, Y.-M. 2020 Settling velocity of porous spherical particles. *J. Hydraul. Engng* **146**, 04019046.

https://doi.org/10.1017/jfm.2025.10919 Published online by Cambridge University Press

ERN, P., RISSO, F., FABRE, D. & MAGNAUDET, J. 2012 Wake-induced oscillatory paths of bodies freely rising or falling in fluids. *Annu. Rev. Fluid Mech.* **44**, 97–121.
FERNANDEZ-PELLO, A.C. 2017 Wildland fire spot ignition by sparks and firebrands. *Fire Safety J.* **91**, 2–10.
FRANKEL, A., POURANSARI, H., COLETTI, F. & MANI, A. 2016 Settling of heated particles in homogeneous turbulence. *J. Fluid Mech.* **792**, 869–893.
GANGULI, S. & LELE, S.K. 2019 Drag of a heated sphere at low Reynolds numbers in the absence of buoyancy. *J. Fluid Mech.* **869**, 264–291.
GANGULI, S. & LELE, S.K. 2020 Drag of a heated sphere at low Reynolds numbers in the presence of buoyancy. *arXiv* p. 2009.09985v1.
GEMMELL, B.J., OH, G., BUSKEY, E.J. & VILLAREAL, T.A. 2016 Dynamic sinking behaviour in marine phytoplankton: rapid changes in buoyancy may aid in nutrient uptake. *Proc. R. Soc. Lond. B* **283**, 20161126.
HAMEL, J.-F., SUN, J., GIANASI, B.L., MONTGOMERY, E.M., KENCHINGTON, E.L., BUREL, B., ROWE, S., WINGER, P.D. & MERCIER, A. 2019 Active buoyancy adjustment increases dispersal potential in benthic marine animals. *J. Animal Ecol.* **88**, 820–832.
HU, S.-Y., WANG, K.-Z., JIA, L.-B., ZHONG, J.-Q. & ZHANG, J. 2021 Enhanced heat transport in thermal convection with suspensions of rod-like expandable particles. *J. Fluid Mech.* **928**, R1.
JAYAWICKRAMA, T.R., HAUGEN, N.E.L., BABLER, M.U., CHISHTY, M.A. & UMEKI, K. 2019 The effect of Stefan flow on the drag coefficient of spherical particles in a gas flow. *Intl J. Multiphase Flow* **117**, 130–137.
KELLEY, D.H. & OUELLETTE, N.T. 2011 Using particle tracking to measure flow instabilities in an undergraduate laboratory experiment. *Am. J. Phys.* **79**, 267–273.
KHATMULLINA, L. & ISACHENKO, I. 2017 Settling velocity of microplastic particles of regular shapes. *Mar. Pollut. Bull.* **114**, 871–880.
KOO, E., PAGNI, P.J., WEISE, D.R. & WOYCHEESE, J.P. 2010 Firebrands and spotting ignition in large-scale fires. *Intl J. Wildland Fire* **19**, 818–843.
KOTOUČ, M., BOUCHET, G. & SUŠEK, J. 2009 Drag and flow reversal in mixed convection past a heated sphere. *Phys. Fluids* **21**, 054104.
MANZELLO, S.L., MARANGHIDES, A. & MELL, W.E. 2007 Firebrand generation from burning vegetation. *Intl J. Wildland Fire* **16**, 458–462.
MANZELLO, S.L., SUZUKI, S., GOLLNER, M.J. & FERNANDEZ-PELLO, A.C. 2020 Role of firebrand combustion in large outdoor fire spread. *Prog. Energy Combust. Sci.* **76**, 100801.
MIYAMURA, A., IWASAKI, S. & ISHII, T. 1981 Experimental wall correction factors of single solid spheres in triangular and square cylinders, and parallel plates. *Intl J. Multiphase Flow* **7**, 41–46.
MOGRABI, E. & BAR-ZIV, E. 2005*a* Dynamics of a spherical particle in mixed convection flow field. *J. Aerosol Sci.* **36**, 387–409.
MOGRABI, E. & BAR-ZIV, E. 2005*b* On the mixed convection hydrodynamic force on a sphere. *J. Aerosol Sci.* **36**, 1177–1181.
OLIVEIRA, L.A., LOPES, A.G., BALIGA, B.R., ALMEIDA, M. & VIEGAS, D.X. 2014 Numerical prediction of size, mass, temperature and trajectory of cylindrical wind-driven firebrands. *Intl J. Wildland Fire* **23**, 698–708.
OR, D., FURTAK-COLE, E., BERLI, M., SHILLITO, R., EBRAHIMIAN, H., VAHDAT-ABOUESHAGH, H. & MCKENNA, S.A. 2023 Review of wildfire modeling considering effects on land surfaces. *Earth-Sci. Rev.* **245**, 104569.
PRATT, K.C. & WAKEHAM, W.A. 1974 The mutual diffusion coefficient of ethanol–water mixtures: determination by a rapid, new method. *Proc. R. Soc. Lond. A* **336**, 393–406.
REYNOLDS, C.S., OLIVER, R.L. & WALSBY, A.E. 1987 Cyanobacterial dominance: the role of buoyancy regulation in dynamic lake environments. *New Zealand J. Mar. Freshwat. Res.* **21**, 379–390.
SÁNCHEZ TARIFA, C., PÉREZ DEL NOTARIO, P. & GARCÍA MORENA, F. 1965 On the flight paths and lifetimes of burning particles of wood. *Proc. Combust. Inst.* **10**, 1021–1037.
THOMAS, C.M., SHARPLES, J.J. & EVANS, J.P. 2020 The terminal-velocity assumption in simulations of long-range ember transport. *Maths Comput. Simul.* **175**, 96–107.
THURSTON, W., KEPERT, J.D., TORY, K.J. & FAWCETT, R.J.B. 2017 The contribution of turbulent plume dynamics to long-range spotting. *Intl J. Wildland Fire* **26**, 317–330.
TOHIDI, A. & KAYE, N.B. 2017 Stochastic modeling of firebrand shower scenarios. *Fire Safety J.* **91**, 91–102.
UHLMANN, M. & DUŠEK, J. 2014 The motion of a single heavy sphere in ambient fluid: a benchmark for interface-resolved particulate flow simulations with significant relative velocities. *Intl J. Multiphase Flow* **59**, 221–243.
WANG, Z., DOU, M., REN, P., SUN, B., JIA, R. & ZHOU, Y. 2021 Settling velocity of irregularly shaped microplastics under steady and dynamic flow conditions. *Environ. Sci. Pollut. Res.* **28**, 62116–62132.

https://doi.org/10.1017/jfm.2025.10919 Published online by Cambridge University Press

YANG, W., WAN, Z.-H., ZHOU, Q. & DONG, Y. 2022 On the energy transport and heat transfer efficiency in radiatively heated particle-laden Rayleigh–Bénard convection. *J. Fluid Mech.* **953**, A35.

ZAMANSKY, R., COLETTI, F., MASSOT, M. & MANI, A. 2016 Turbulent thermal convection driven by heated inertial particles. *J. Fluid Mech.* **809**, 390–437.

https://doi.org/10.1017/jfm.2025.10919 Published online by Cambridge University Press